RESEARCH ARTICLE

ADVANCED OPTICAL MATERIALS
www.advopticalmat.de

The Role of Optical Centers in Neodymium-Doped Calcium Fluoride: Optical Tagging and Nanothermometry in the Second Biological Window

*Pablo Camarero, Rosalía López-Méndez, Diego Lecumberri Díez, Patricia Haro-González, Eugenio Cantelar, and Marta Quintanilla**

Nd^{3+} has been proposed for nanothermometry in biological media, as both its emission and excitation wavelengths fall within the regions of low attenuation in tissues. While most crystal hosts only allow for thermometry through the low-intensity emission near 900 nm, CaF_2 enables intraband thermometry at the highest intensity emission band, ≈1042 nm. The incorporation of Y^{3+} ions into CaF_2:Nd^{3+},Y^{3+} nanoparticles enhances the emission intensity of Nd^{3+}. However, this also induces significant modifications in the spectral lineshape, which are detrimental to thermometry, as the required peaks needed to define a reliable thermometric ratio are eliminated at $[Y^{3+}] > 10$ mol%. In this study, we demostrate that this limitation depends on the excitation wavelength, as three different optical centers can be selectively activated by tuning it within a narrow range (<6 nm), with profound implications for the emission spectra. The fact that optical centers can be differentiated in nanoparticles even at room temperature can be exploited to recover the thermometric ability even with high $[Y^{3+}]$ concentrations, thus providing nanothermometers with potentially better signal-to-noise ratios.

1. Introduction

The optical properties of lanthanide-doped nanoparticles distinguish them as a differentiated category of nanomaterials particularly suited for optical tagging and sensing. Their emission arises from transitions between 4*f* states, which are partially shielded from the environment by outer electronic layers. This results in a weak dependence on the crystal host, as well as on the solvent´s composition, ionic strength, and pH. Besides, electronic shielding also involves that the emission bands of lanthanides are distinctively narrow.

In the context of sensing applications, the weak influence of the surrounding medium minimizes potential errors in the measurements, often caused by interactions with uncontrolled concentrations of molecules. In addition, the narrow and well-defined emission bands facilitate deconvolution from other luminescent signals. This is particularly advantageous in heterogeneous environments, such as biological tissues, in which the medium presents endogenous luminescence known as autofluorescence.[1,2]

It is largely due to these applications that lanthanide-doped nanoparticles have been studied and developed. Still, their practical use is limited, as their emission quantum yield is lower than that of other luminescent nanomaterials, including organic dyes, quantum dots, or carbon dots, to cite some.[3–6] These alternative materials, while often brighter, also present drawbacks, including low stability, toxicity, or sensitivity to the compositional characteristics of the solvents. Consequently, each material is adequate for specific situations, but none offers universal applicability across all sensing scenarios.[7] Regarding lanthanide-doped nanoparticles, a central challenge is to enhance emission intensity. Achieving this requires a comprehensive understanding of the materials, aiming to handle their properties and minimize the sources of luminescence quenching.[8–11]

Notably, the emission quantum yield of bulk materials is typically higher than that of the nanoparticulate counterparts.[12,13] Indeed, emission quantum yield has been shown to be a size-dependent characteristic, which often lowers as size decreases,[12–14] though some exceptions exist.[15]

The mechanisms underlying these changes at the nanoscale are still a matter of debate, despite the relevance of this information to optimizing the material properties. Yet, several aspects are already known. For instance, nanoparticles smaller than 20 nm

P. Camarero, D. Lecumberri Díez, P. Haro-González, E. Cantelar, M. Quintanilla
Materials Physics Department
Universidad Autónoma de Madrid
Avda. Francisco Tomás y Valiente 7, Madrid 28049, Spain
E-mail: marta.quintanilla@uam.es

P. Camarero, R. López-Méndez, D. Lecumberri Díez, P. Haro-González, E. Cantelar, M. Quintanilla
Nicolás Cabrera Institute
Universidad Autónoma de Madrid
Avda. Francisco Tomás y Valiente 7, Madrid 28049, Spain

R. López-Méndez
IMDEA Nanociencia
C/ Faraday, 9, Madrid 28049, Spain

The ORCID identification number(s) for the author(s) of this article can be found under https://doi.org/10.1002/adom.202501200

DOI: 10.1002/adom.202501200

exhibit a discrete phonon density of states (PDOS), while low-frequency phonons are cut off.[16] These alterations affect non-radiative and phonon-assisted energy transfer probabilities. As a consequence, a different emission color as nanoparticles become smaller can be observed.[16,17]

However, this is not the only change linked to size reduction. The surface region, which may extend 5–10 nm into the nanoparticle,[6,8] becomes more relevant as the material becomes smaller. It typically presents altered crystal lattice parameters and a higher density of defects compared to the bulk. This creates different local symmetries for the lanthanide dopants, affecting their emission intensity, but also producing different emission lines at slightly shifted wavelengths.[10,16] In addition, the adsorption of OH^- or CO_3^{2-} anions has been shown to induce luminescence quenching to lanthanide ions.[18–20] Thus, the characteristics of the surface layer include structural and electronic differences which may trigger changes in the emission lifetimes, transition probabilities, and generate broader emission bands.[19,21]

Motivated by the possibilities that a complete understanding of lanthanide-doped nanomaterials may open in terms of improving their luminescence for applications, in this work, we address the optical properties of CaF_2:Nd^{3+},Y^{3+} nanoparticles. The bulk material has been carefully described in the past, largely due to its interest as a laser material.[22–24] Recently, CaF_2 has been found to be a relevant host for lanthanides also in nanoparticles in the context of optical sensors, and thus synthesis strategies have been developed.[25,26] Particularly interesting is the doping with Nd^{3+}, as the ion can be excited at wavelengths ≈800 nm ($^4I_{9/2} \rightarrow {}^4F_{5/2}$, $^2H_{9/2}$) and presents its main emission at ≈1050 nm ($^4F_{3/2} \rightarrow {}^4I_{11/2}$), being both emissions located in the ranges in which biological tissues have a lower optical attenuation (known as biological windows). Specifically, the mentioned excitation wavelength lies within the first biological window, while the emission lies within the second one.[25,27] Given this fact, it arises as a relevant material for optical tagging and has indeed been used to analyze the diffusion of photothermal probes inside 3D tumor spheroids.[28] The emission intensity near 1050 nm has also been shown to be useful for nanothermometry. Such an option is based on the transitions between different Stark sublevels, providing peaks with different thermal dependencies; thus, the intensity ratio between them becomes a reliable parameter for thermal sensing.[25,28]

Efforts to enhance its emission intensity are especially relevant in the context of biomedical applications, as excitation power needs to be limited to avoid tissue damage and reduce autofluorescence, mainly from melanin.[29] Particularly, it has been shown that the addition of Y^{3+} ions increases the emission intensity of Nd^{3+} in CaF_2.[30] Such improvement involves a better signal-to-noise ratio of the recorded luminescence, and thus a better chance to use the nanoparticles as tags or sensors. However, the presence of Y^{3+} also alters the spectral lineshape to the extent that, for instance, the thermometric ability of the material disappears if it is added at a concentration above 10 mol% in samples with 1 mol% Nd^{3+}.[25]

In this work, applying site selection spectroscopy techniques, we have observed that it presents clearly differentiated optical centers, an unusual feature to be observed at room temperature, especially in nanoparticles. This possibility, though, is possible in CaF_2.[31] Thanks to this characteristic, two distinct emissions can be tuned by carefully selecting the excitation wavelength. The obtained results are compared with those published for the bulk material, to understand how doped-CaF_2 system keeps its properties at the nanoscale. Then, with our mind set on the sensing application, we have studied how to benefit from the presence of optical sites to improve both intensity and thermal sensitivity.

2. Results

The nanoparticles have been synthesized following a hydrothermal route in a pressurized reactor autoclave.[32] The obtained nanoparticles present a homogeneous cubic shape (**Figure 1**; Figures S1 and S2 of the Supporting Information). The size distribution has been analyzed using as dimensional parameter the diagonal length of the square, which has been measured in more than 500 particles per sample. The obtained results (Figure 1; Figures S1 and S2, Supporting Information) are fit to a log-normal distribution to determine the most frequent size.[33] The error is defined as the half-width at half maximum. Results, given in **Table 1**, show that all samples present a diagonal length between 11 and 13 nm.

Homogeneity is key in this study, as in lanthanide-doped nanoparticles, surface effects can strongly affect the luminescent properties of the dopants, and their relevance strongly depends on size. Another relevant characteristic of the nanoparticles that may have profound implications for their luminescent properties is dopant concentration. To check that all rare earth ions added to the synthesis were incorporated into CaF_2 crystals, TXRF experiments were conducted. The concentration of dopants measured in this way is listed in Table 1, which shows that the final Y^{3+} concentration closely matches the expected value, while Nd^{3+} concentration is 0.9 mol% rather than 1mol%, a value that remains fairly constant across the sample set. Only in two samples is the concentration of Nd^{3+} slightly deviated from this value ($[Y^{3+}] = 1$ mol% and, to a lesser extent, $[Y^{3+}] = 15$ mol%). In such cases, this information needs to be kept in mind when optical properties are discussed, as it may produce deviations.

XRD diffractograms, shown in **Figure 2**A together with the expected diffraction angles of cubic CaF_2, indicate that the nanoparticles present a cubic lattice structure, which is consistent with the observed shape. Besides this general information, XRD data allow for a more detailed analysis of the nanoparticles, including crystallite size and lattice parameters. These features were analyzed by performing a Rietveld fit of the diffractograms (details regarding the fit are available in Section 2 of the Supporting Information), which offer the results summarized in Table 1. First, a comparison of the crystallite size and the dimensions measured through TEM images confirms that the nanoparticles are monocrystalline, which emphasizes their homogeneity. Second, the lattice parameter monotonically grows as the concentration of dopants increases (for interested readers, data are plotted in Figure S4, Supporting Information), indicating that the rare earths induce a certain lattice expansion. Following this trend, the obtained values are consistent with previous lattice parameters reported for pure CaF_2 nanoparticles (5.4617 Å).[34] The observed lattice expansion is consistent with the distortions that doping triggers in the crystal, including the appearance of interstitial F^- ions for charge compensation.

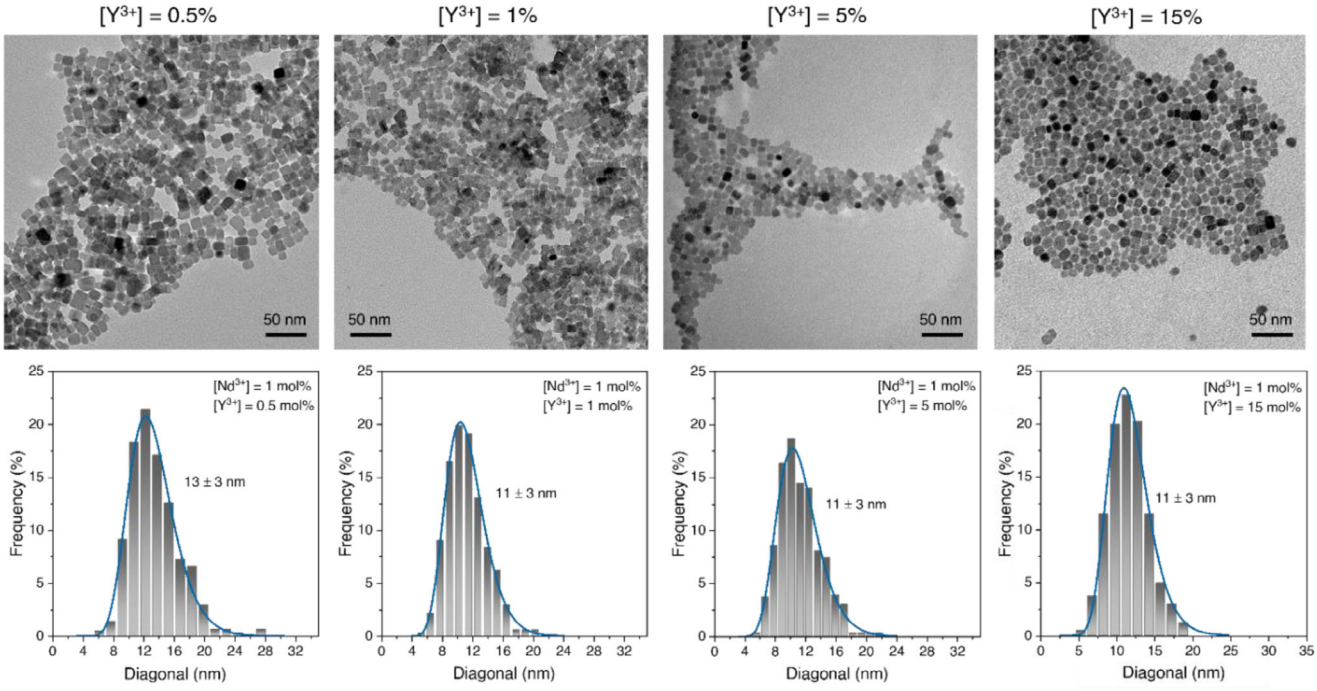

Figure 1. TEM micrographs showing the size and morphology of the samples. The size distribution is added below, fit to a log-normal function to determine the most frequent nanoparticle diagonal dimension.

2.1. General Emission Properties

Neodymium ions are characterized by having several emission bands in the near-infrared range, which can be excited at ≈800 nm, in the spectral range in which biological tissues present a lower light attenuation. The inset of Figure 2B shows a partial diagram of Nd^{3+} energy states, indicating the different possible transitions and the related emission wavelength. As seen, excitation at ≈800 nm can promote an electron from $^4I_{9/2}$ state up to $^4F_{5/2}$ and $^2H_{9/2}$ states. A subsequent non-radiative relaxation would then populate $^4F_{3/2}$ state, which is responsible for three near-infrared emission bands at ≈900, ≈1050, and ≈1300 nm. Figure 2B shows the emission spectrum obtained from exciting CaF_2:Nd^{3+} (1 mol%) sample at 808 nm, with the three mentioned bands. The highest intensity is found at 1042 nm, which corresponds to $^4F_{3/2} \rightarrow {}^4I_{11/2}$ transition. In addition, the emissions related to $^4F_{3/2} \rightarrow {}^4I_{9/2}$ and $^4F_{3/2} \rightarrow {}^4I_{13/2}$ transitions are observed, though they present lower intensities.

Optical sensing, and specifically nanothermometry, benefits from intense emissions, as they guarantee a lower signal-to-noise ratio. Thus, exploiting the emission related to $^4F_{3/2} \rightarrow {}^4I_{11/2}$ is in principle the preferred choice. Such nanothermometry possibility has been demonstrated in CaF_2:Nd^{3+} using the ratio between the intensity at 1042 nm and the intensity at 1062 nm, which appears as a secondary peak in the spectrum of Figure 2B.[25] Many other hosts have been proposed for Nd^{3+}-based thermometry. However, they are often based on the intensity ratio between spectrally distant emission bands or on the less intense emission at ≈870 nm ($^4F_{3/2} \rightarrow {}^4I_{9/2}$), as in most hosts, $^4F_{3/2} \rightarrow {}^4I_{11/2}$ emission, despite being more intense, does not show a good thermal sensitivity, or doesn´t present the sharp structure of peaks observed in CaF_2.[35–43] Indeed, there are very few examples, besides

Table 1. Size, dopant concentration, and crystal properties of the obtained samples. Concentration is given as mol%, and size refers to the diagonal dimension of the nanoparticles. Crystallite size and lattice parameters are obtained from Rietveld analyses.

Expected Concentration [mol%]	Measured Concentration [mol%]	Nanoparticle Size [nm]	Crystallite Size [nm]	Lattice Parameter, a = b = c [Å]
$[Nd^{3+}]$ = 1%, $[Y^{3+}]$ = 0%	$[Nd^{3+}]$ = 0.9%, $[Y^{3+}]$ = 0.0%	11 ± 3	12.1 ± 0.9	5.4653 ± 2.10^{-4}
$[Nd^{3+}]$ = 1%, $[Y^{3+}]$ = 0.5%	$[Nd^{3+}]$ = 0.9%, $[Y^{3+}]$ = 0.6%	13 ± 3	13.2 ± 0.1	5.4655 ± 2.10^{-4}
$[Nd^{3+}]$ = 1%, $[Y^{3+}]$ = 1%	$[Nd^{3+}]$ = 0.6%, $[Y^{3+}]$ = 1.1%	11 ± 3	11.8 ± 0.5	5.4658 ± 2.10^{-4}
$[Nd^{3+}]$ = 1%, $[Y^{3+}]$ = 5%	$[Nd^{3+}]$ = 0.9%, $[Y^{3+}]$ = 5.5%	11 ± 3	10.9 ± 0.4	5.4668 ± 2.10^{-4}
$[Nd^{3+}]$ = 1%, $[Y^{3+}]$ = 10%	$[Nd^{3+}]$ = 0.9%, $[Y^{3+}]$ = 10.5%	12 ± 3	9.5 ± 0.7	5.4685 ± 2.10^{-4}
$[Nd^{3+}]$ = 1%, $[Y^{3+}]$ = 15%	$[Nd^{3+}]$ = 0.7%, $[Y^{3+}]$ = 16.1%	11 ± 3	12.8 ± 0.6	5.4699 ± 2.10^{-4}

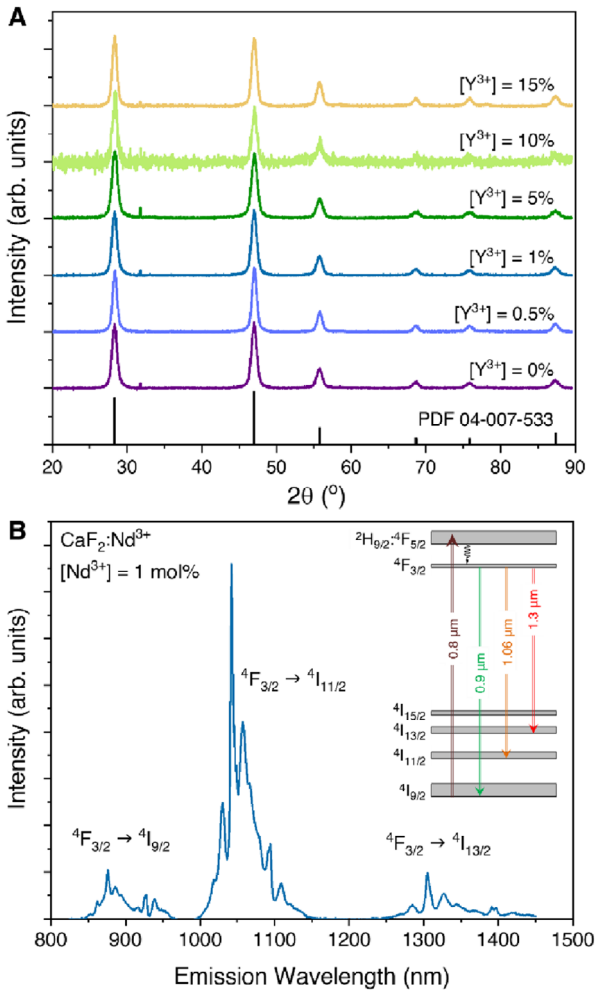

Figure 2. A) XRD diffractograms of the prepared samples together with the reference for cubic CaF_2. B) Energy level diagram of Nd^{3+} and emission spectrum obtained after excitation at 808 nm in a sample with $[Nd^{3+}] = 1$ mol%.

CaF_2,[25] in which the most intense transition has been used for thermal sensing.[44,45] This indicates that thermal sensing using this emission must be connected with the effect of the host on Nd^{3+} luminescence.

Aiming to further improve the intensity of Nd^{3+} emissions, Y^{3+} can be added to the material. The reasoning for this strategy takes into account that both ions will enter the lattice in the same sites, and relies on CaF_2 crystal structure and on the structural changes forced by RE^{3+} ions when they enter the lattice. In this host, RE^{3+} dopants occupy Ca^{2+} positions in the crystal, inducing the appearance of an interstitial F^- ion as a charge compensation mechanism (**Figure** 3A). The appearance of this interstitial F lowers the symmetry of the optical sites and thus is key to increasing the dopant emission intensity of lanthanides. There are several possible locations for this F^-, which implies that more than one optical center constituted by a RE^{3+}-F^- pair, called L center, is possible. In the case of Nd^{3+} it has been theoretically shown that the most stable situation has the interstitial F^- in the nearest-neighbor position, which forms tetragonal C_{4v} optical sites.[46] For very low Nd^{3+} concentrations, these optical centers dominate. Yet, if the concentration of Nd^{3+} ions surpasses 0.06 mol% new optical centers with C_s symmetry appear. These new centers are related to the presence of clusters with two or four Nd^{3+} ions, together with their corresponding two or four interstitial F^- ions.[47] These centers, respectively labelled as M and N centers (Figure 3B,C), become more frequent as Nd^{3+} concentration is further increased, dominating absorption and emission spectra for concentrations as low as ≈0.6 mol%.

From the luminescence point of view, the existence of clusters creates new emission lines. However, they may also reduce the overall emission intensity of Nd^{3+} ions by increasing the probability of migration processes, which subsequently increases the probability of non-radiative relaxations. Alternatively, cross-relaxation processes between Nd^{3+} ions are also enhanced at higher concentrations, and thus can deplete the excited state.[48] These two mechanisms, being based on energy transfer, are strongly dependent on the distance between ions. Thus, if Y^{3+} ions are intercalated between Nd^{3+} ions, they can help to improve emission intensity, as they increase the distance between Nd^{3+} ions and don´t introduce additional energy levels in this range. Also, as RE^{3+}, they enter the same sites as Nd^{3+} ions do, participating in M and N centres. To differentiate the new Y^{3+}-containing centers, they are renamed as M' and N' centers, with an apostrophe.[49]

To study the effect of Y^{3+} on luminescence, a sample series with variable Y^{3+} concentration (from 0 mol% up to 15 mol%) but constant Nd^{3+} (1 mol%, thus already having clusters) was prepared. After excitation at 808 nm, the intensity of the three emission bands in Figure 2B is found to increase with Y^{3+} concentration (**Figure 4**). This intensity change is subtle for the lower Y^{3+} concentrations and becomes stronger for $[Y^{3+}] > 5$ mol%. In Figure 4 it is also clear that a change of the spectral lineshape takes place. This has a direct effect on optical sensing options based on intraband intensity ratios, since peaks involved in the ratio disappear at higher emission intensities.[25]

To gain a deeper understanding of the emission behavior, the excitation spectra of the samples with the lowest and highest Y^{3+} content are plotted in Figure 4D,E. The spectra first reveal that the commonly used excitation in biomedical applications, 808 nm, is not resonant with the excitation maximum. This suggests that a significant increase in intensity may be achieved by slightly shifting the excitation wavelength. Second, as observed with the emissions in Figure 4A–C, the excitation spectra also exhibit a markedly different lineshape at varying concentrations. This means that the situation at low and high Y^{3+} concentrations differs too significantly to establish a fixed intensity ratio applicable to all samples. Indeed, it is likely that each sample requires a different excitation wavelength to optimize its thermometric performance.

2.2. Optical Centers in Nanoparticles

Such a spectral change points toward the existence of different optical centers in each sample, formed upon the addition of Y^{3+}. Particularly, following the previous description, the spectra in Figure 4 should have a larger contribution of M' and N' centers as Y^{3+} concentration is increased. However, the incorporation of

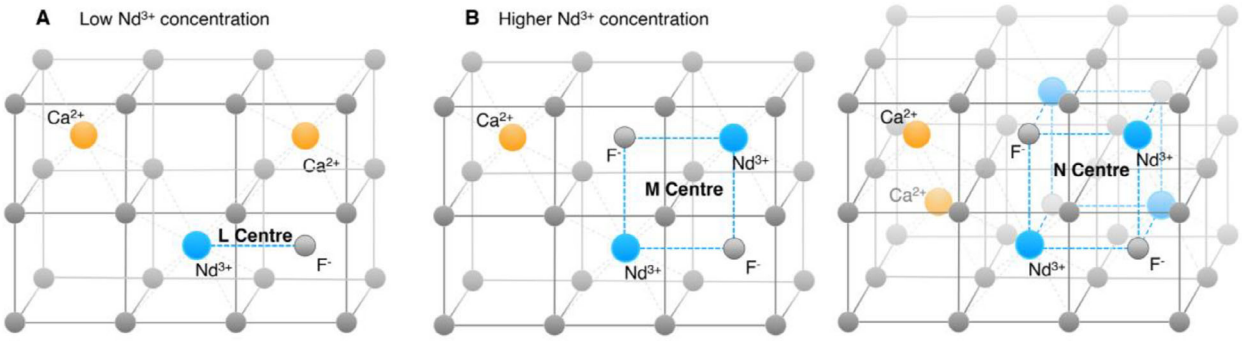

Figure 3. CaF_2 crystal lattice with Nd^{3+} inclusions. Three configurations are often described, being their frequency dependent on Nd^{3+} concentration. A) Nd^{3+}-F^- pairs, constituting L centers, dominate for concentrations below 0.06 mol%. For higher concentrations, M centers (B) and N centers (C) appear.

Y^{3+} has been described to have additional microscopic effects that may affect luminescence,[49] including:

- The appearance of an L′ center, consisting of a Nd^{3+} with two interstitial F^- associated. This is possible because, different than Nd^{3+}, Y^{3+} dopants are likely to create the interstitial F^- at longer distances than the nearest-neighbor. This favors their interaction with Nd^{3+} ions and reduces the frequency of Y^{3+}-F^- pairs.[46]
- Nd^{3+} coordination number increases beyond 8, reaching almost 11 upon Y^{3+} incorporation (at least up to a 5 mol%). This favors the appearance of a larger number of F^- ions in its surroundings.
- The crystal lattice expands, thus increasing Nd-F distances.
- Higher dopant content favors short-range lattice disorder.

Even though the available description of optical centers has been developed for bulk CaF_2, nanoparticles may also include these centers, but with their properties probably distorted by surface effects. This may include broadening of emission peaks and unsharpened spectral lineshapes. Motivated to find a strategy to improve the properties of the material as a thermal sensor, we aim to further understand the spectra in Figure 4 using the information of the bulk as a reference. For the analysis, we focus on the direct excitation of $^4F_{3/2}$ state, as the lower number of Stark sublevels may facilitate a direct comparison.

To obtain an overview of the emission peaks and their excitation spectra, luminescence was recorded with 1 nm step by exciting at different wavelengths between 833 and 895 nm (1.85 nm step). The obtained spectra are shown in **Figure** 5A–C as contour maps, being the coordinates being the emission (x-axis) and excitation (y-axis) wavelengths. In the figure, three samples with different Y^{3+} concentrations are presented, though the full set of samples is available in the SI (Figures S5 and S6, Supporting Information). In agreement with Figure 4, as Y^{3+} concentration increases, the spectral shape changes, both in emission and excitation.

For comparison Figure 5D–F show three emission spectra for each sample, excited at selected relevant wavelengths: 840.5 nm, corresponding to the spectral tail; 857.3 nm, a secondary excitation maximum for the $[Y^{3+}] = 15\%$ sample; and 862.9 nm, the absolute excitation maximum of the same sample (complete series of emission spectra at different wavelengths are provided in the Supporting Information as Figures S7 and S8). It must be noted that this latest wavelength is close to the maximum excitation in the sample without Y^{3+} content, but not the same. Specifically, the main excitation peak of the sample without Y^{3+} is slightly blue-shifted and appears at 860.7 nm.

Focusing on the sample with the lowest Y^{3+} concentration (i.e., 0 mol%) all spectra show the same lineshape regardless of the excitation wavelength. Instead, as Y^{3+} concentration is increased, different emission lineshapes appear depending on the exact excitation wavelength. Indeed, for $[Y^{3+}] = 15$ mol%, two different emission spectra can be obtained by changing the excitation wavelength in only 5.6 nm (from 857.3 to 862.9 nm), and these are different from the lineshape obtained when excited at the lower intensity range (840.5 nm). Such a behavior is characteristic of samples with several optical centers that can be selectively tuned through excitation. These optical centers must be linked to the presence of Y^{3+}, as without it, no dependence on the excitation is observed.

Spectroscopic observation of optical centers in nanoparticles is uncommon, given the pronounced influence of surface effects and crystal defects on the emission, which leads to peak broadening. Here, though, this is observed even at room temperature, which is probably due to the very specific structure of CaF_2-doped crystals. Thinking along this line, the presence of such optical centers is probably behind the fact that this is one of the very few crystal hosts that allows defining intensity ratios to measure temperature in the emission band with the highest intensity ($^4F_{3/2} \rightarrow {}^4I_{11/2}$), while most other materials can only exploit the less intense band linked to $^4F_{3/2} \rightarrow {}^4I_{9/2}$ transition.[35–42]

To further describe the situation and check whether these emission characteristics are triggered by the presence of optical centers, the main emission lines reported for bulk CaF_2:Nd^{3+} have been compared with the obtained spectra.[47,50] This involves calculating the energies of the transitions between the Stark sublevels of each state. This is, in the excitation, from the ground state (Z_1 to Z_3) to the excited state (R_1 and R_2); and in the emission, from these same excited state sublevels to the only sublevel Y_1. The calculated wavelengths are shown in **Figure** 6A for the sample without Y^{3+} (purple lines label transitions related to R_2 and orange lines label transitions related to R_1). Although the reported lines were measured at 10K, which is not the case

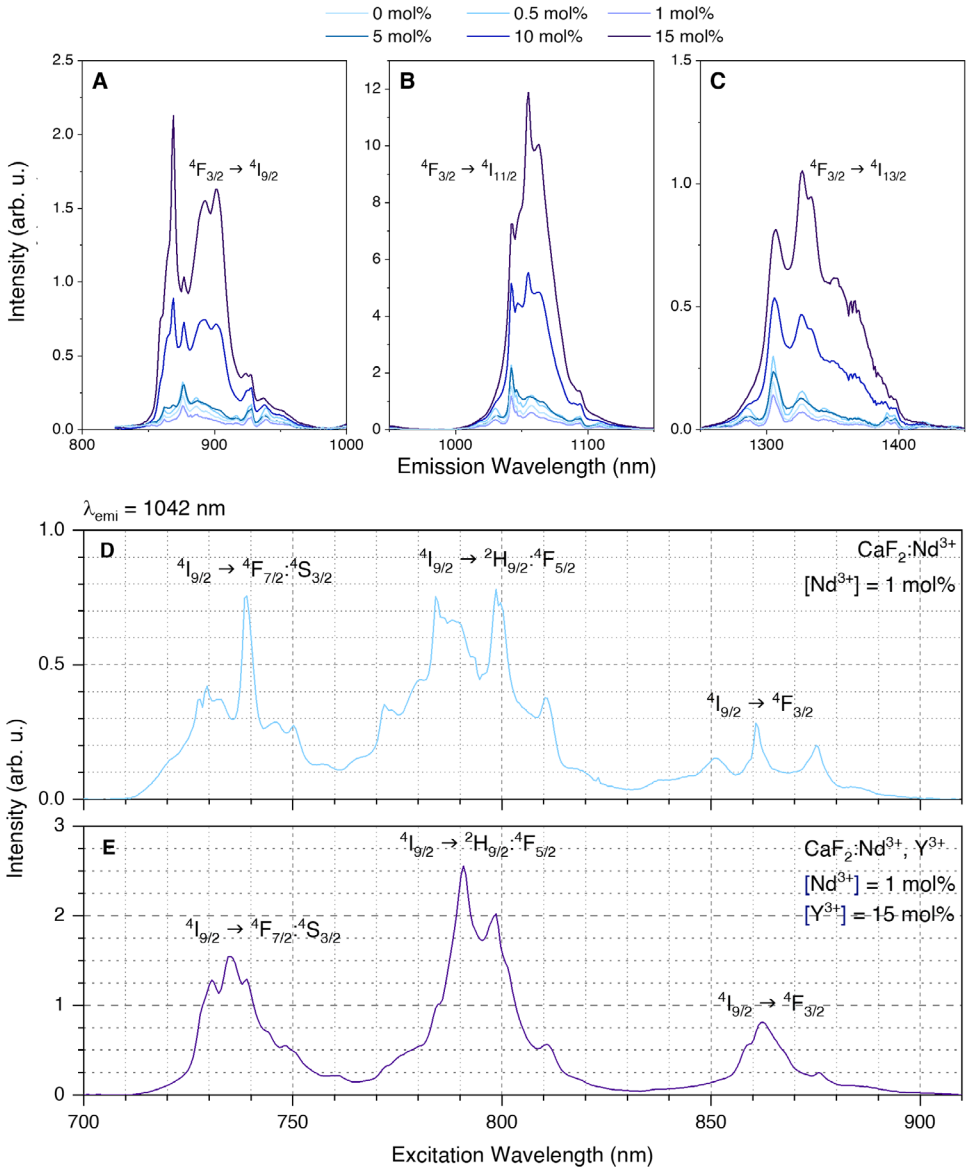

Figure 4. Emission bands of Nd^{3+} ions at 1 mol% in CaF_2 nanoparticles containing also different Y^{3+} contents, and excited at 808 nm. The bands correspond to $^4F_{3/2} \rightarrow {}^4I_{9/2}$ transition (A), $^4F_{3/2} \rightarrow {}^4I_{11/2}$ transition (B) and $^4F_{3/2} \rightarrow {}^4I_{13/2}$ transition (C). Excitation spectra of the main emission line (at 1042 nm) of a sample with $[Nd^{3+}]$ = 1 mol% and no Y^{3+} (D) or 15 mol% Y^{3+} (E).

here, there is a clear match of excitation expected lines with the measured spectrum, suggesting that in the absence of Y^{3+}, emission is dominated by L centers. In the case of the emission, instead, a small shift of the emission bands is observed, as compared to the reported lines. The lattice parameters of CaF_2 nanoparticles (Table 1) are slightly different than those in bulk, which can trigger a distortion that causes such a shift. Still, the observed match is clear enough to support the prevalence of L centers. For the sake of completeness, the contribution of more complex centers should be considered here as well (see Figure S9, Supporting Information) for the equivalent of Figure 6A). Their contribution cannot be totally disregarded, but if any, it must be minor, considering the lack of main peaks in agreement with the expected energies.

The same strategy applied to the sample with $[Y^{3+}]$ = 15 mol% is not as conclusive. The shift created by the distorted lattice of the nanoparticles sums up to the fact that a higher presence of M and N centers is likely, producing the overlap of the spectral lines, which cannot be totally deconvoluted. Besides, in this case, L', M', and N' must be considered instead, but the information available on these centers is not as detailed as in the case of their simpler counterparts.[22,49,51] Still, the available description indicates that N' is preferentially excited at ≈859 nm, while M' requires slightly longer wavelengths (between 860 and 863 nm). A close inspection of Figure 5C shows that there are two clear sets of emission peaks, one excited at ≈863 nm, and another one excited at 857 and 868 nm, which aligns with the published information. However, the first emission peak at 1042 nm, appearing with different

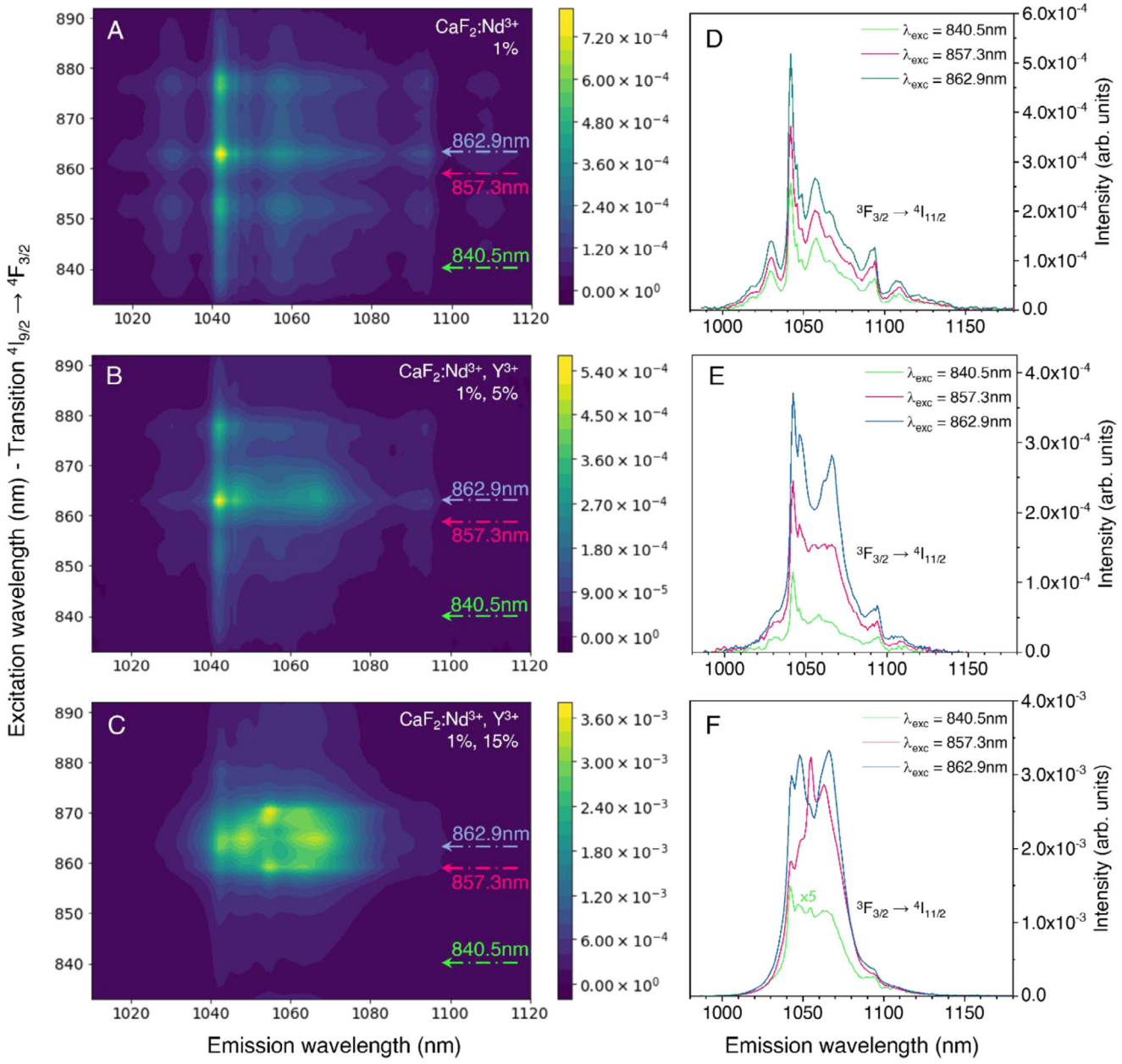

Figure 5. Emission spectra corresponding to the $^3F_{3/2} \rightarrow {}^4I_{11/2}$ transition as a function of excitation of the $^4I_{9/2} \rightarrow {}^4F_{35/2}$ transition are presented as intensity contour maps of the samples without Y^{3+} (A), with $[Y^{3+}] = 5$ mol% (B), and with $[Y^{3+}] = 15$ mol% (C). Emission spectra measured at three distinct excitation wavelengths – 840.5 nm, 857.3 nm, and 862.9 nm – are shown for the same three samples in D ($[Y^{3+}] = 0$ mol%), E ($[Y^{3+}] = 5$ mol%), and F ($[Y^{3+}] = 15$ mol%).

intensities in both excitation options, can also be excited separately (see excitation at 840.2 nm), which reveals the presence of a third centre. Consequently, at room temperature the different centres cannot be fully isolated by changing the excitation wavelength, although following the literature, the spectrum obtained after excitation at 857.3 nm (pink in Figure 5C) is probably dominated by N' centres, while the one obtained after excitation at 862.9 nm (blue in Figure 5C), is probably dominated by M' centres. Nevertheless, as M' and N' spectra cannot be totally isolated, from now on we will label spectra resembling the blue lineshape as Type-A, and those resembling the pink lineshape as Type-B.

Then, the 1042 nm peak has a likely contribution from L' (or L) centres, as it appears at the same wavelength as the maximum emission of the sample without Y^{3+}. To check this hypothesis, we have selected excitation and emission wavelengths at which this band dominates. This is, $\lambda_{exc} = 875.1$ nm and λ_{emi} between 1000 and 1042 nm. Then, we have done the same for the spectra with more complex optical sites (clusters), which we cannot unentangle, using $\lambda_{exc} = 862.9$ nm and the emission range between 1065

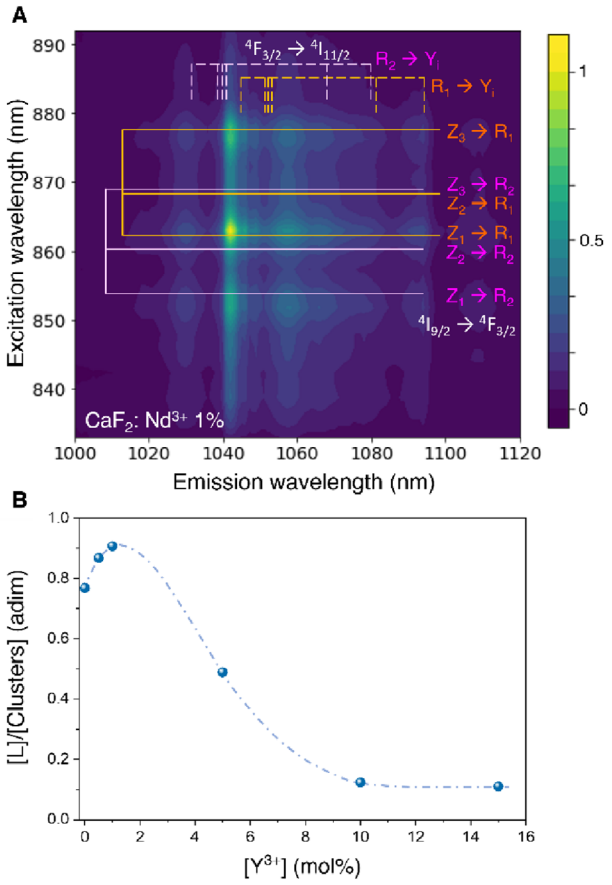

Figure 6. Emission spectra of $^3F_{3/2} \rightarrow {}^4I_{11/2}$ transition after excitation at $^4I_{9/2} \rightarrow {}^4F_{3/2}$ transition of the sample without Y^{3+} plotted in an intensity contour map. The expected positions of the transitions between Stark sublevels are indicated following the bulk material spectral characterization (A).[47,50] Ratio of the emission band assigned to L-Centers versus the emission of more complex centers related to clusters at different [Y^{3+}]. The line is added as a guide to the eye and doesn´t have physical meaning (B).

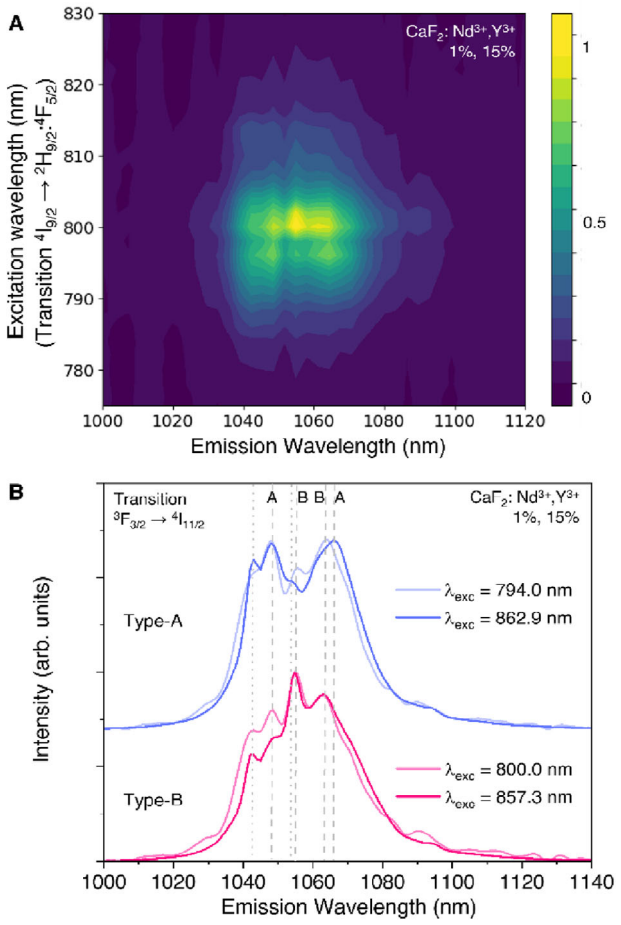

Figure 7. Intensity contour maps of $^3F_{3/2} \rightarrow {}^4I_{11/2}$ emission in the sample with [Y^{3+}] = 15 mol% after excitation at $^4I_{9/2} \rightarrow {}^2H_{9/2}$: $^4F_{5/2}$ transition A). Emission spectra of the same sample at four different excitation wavelengths, selected as they are representative of two characteristic lineshapes, labelled as type-A and type-B. The predominant peaks in each one are indicated with vertical grey dashed lines.

and 1100 nm. Then, in Figure 6B we plot the ratio of the integrated areas of L-centres versus complex centres, demonstrating how they start playing a role at [Y^{3+}] ≈1 mol% and dominate at higher concentrations.

2.3. Thermometry

The detailed spectroscopic characterization just presented used the excitation related to $^4I_{9/2} \rightarrow {}^4F_{3/2}$ transition, at ≈860 nm, because the lower number of sublevels is beneficial to unentangle the optical centers. However, for thermometry, the rationale is different, as now excitation wavelength must improve the emission intensity. Accordingly, the transition $^4I_{9/2} \rightarrow {}^2H_{9/2}$:$^4F_{5/2}$, excited at ≈790 nm, will be chosen from now on. Prior to the thermal analysis, **Figure** 7A presents the spectral map obtained in the excitation range that tunes $^4I_{9/2} \rightarrow {}^2H_{9/2}$:$^4F_{5/2}$. Though the map is clearly different from the one in Figure 5C regarding excitation, emission lines closely resemble the previous ones, as the same optical centers are causing them. To allow comparison, Figure 7B shows the two main emission lineshapes obtained (light colored), and those previously analyzed, exciting at $^4I_{9/2} \rightarrow {}^4F_{3/2}$ (dark colored). The spectra are different, confirming the mixing of M' and N' centers. However, this comparison also shows how some peaks can be specifically prioritized at exact wavelengths, forming the two differentiated lineshapes. As mentioned before, overlapped spectral contributions cannot be fully deconvoluted at room temperature. However, partial identification of the main emissions is possible by fitting the different lineshapes to Gaussian functions (Figure S10 and Table S1, in the Supplementary Information). This analysis reveals at least three overlapping spectra: one from L-centers and two more intense peak sets associated with the optical centers emerging at higher dopant concentrations. It also clarifies the main transitions related to each spectral lineshape.

From a practical point of view, thinking of nanothermometry, the presence of such a diversity of optical centers means that thermal sensitivity will depend on the excitation wavelength, and not only on the concentration of dopants, as previously reported.[25] Also, different optical centers may behave differently with temperature, which may open the way to new strategies.

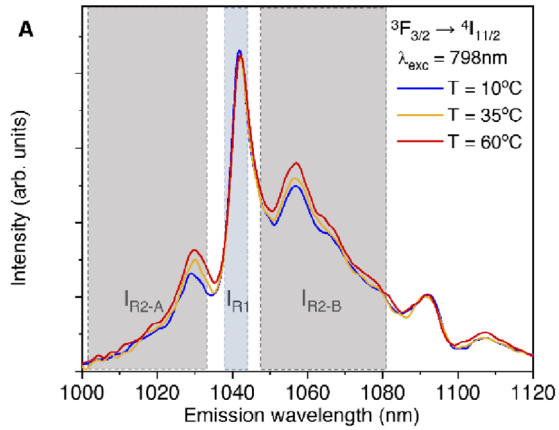

B

Mostly R2 \ Mostly R1	1 peak (1036 – 1042 nm)	2 peaks +(1090-1097 nm)
1 peak, I_{R2-B} (1047 – 1082 nm)	R = 0.97 ΔE = 136 cm^{-1} Sr_{exp} = 0.21 %°C^{-1} Sr_{lin} = 0.21 %°C^{-1}	R = 0.86 ΔE = 121 cm^{-1} Sr_{exp} = 0.18 %°C^{-1} Sr_{lin} = 0.19 %°C^{-1}
2 peaks, I_{R2-A} +(1000 – 1033 nm)	R = 0.98 ΔE = 170 cm^{-1} Sr_{exp} = 0.27 %°C^{-1} Sr_{lin} = 0.26 %°C^{-1}	R = 0.94 ΔE = 163 cm-1 Sr_{exp} = 0.25 %°C^{-1} Sr_{lin} = 0.25 %°C^{-1}
3 peaks +(1098 – 1120 nm)	R = 0.98 ΔE = 183 cm^{-1} Sr_{exp} = 0.28 %°C^{-1} Sr_{lin} = 0.28 %°C^{-1}	R = 0.93 ΔE = 168 cm^{-1} Sr_{exp} = 0.26 %°C^{-1} Sr_{lin} = 0.27 %°C^{-1}

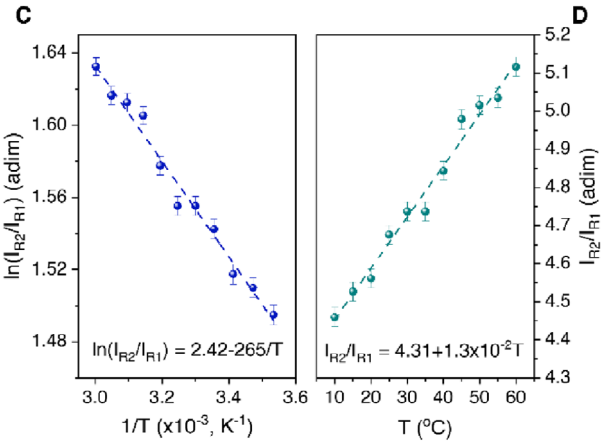

Figure 8. Evaluation of the thermometric options of the sample without Y^{3+}. Emission spectra measured at different temperatures A). Evaluation of the different integrating options to define the thermometer B). The best alternatives are shaded in green, while the worst appear in red and intermediate ones in yellow. Using the best option (framed in green in B, and indicated as shaded grey areas in (A), a thermometer is calibrated. The calibration, considering a Boltzmann distribution, is plotted in (C), while a linear tendency is considered in (D).

In the case of L centers, visible at low [Y^{3+}], the exact excitation wavelength does not play a role in the emission lineshape (Figure 5A). Thus, only one main excitation wavelength (798 nm) has been selected for the thermal analysis. Three spectra measured at different temperatures (T = 10, 35, and 60 °C) are shown in **Figure** 8A, and demonstrate that emission is sensitive to temperature. This can be explained as the crystal field splits $^4F_{3/2}$ state into two sublevels (R_2 and R_1), each emitting at slightly different wavelengths.[47,50] The observed spectral modifications triggered by temperature relate to the redistribution of the electronic population between both sublevels. As R_1 and R_2 are energetically close, electrons can move from the lower to the upper state owing to their thermal energy even at room temperature. In this situation, rapid decay rates from the upper to the lower state imply that the electronic population follows a Boltzmann distribution, with the consequence that the ratio between the intensities emitted by R_1 and R_2 (I_{R1} and I_{R2}, respectively) exponentially depends on 1/T:

$$\frac{I_{R2}}{I_{R1}} = Bexp\left(-\frac{\Delta E}{k_B T}\right) \quad (1)$$

In Equation (1), ΔE is the energy gap between R_1 and R_2, k_B is Boltzmann's constant, and the pre-exponential factor, B, is a constant that depends on spectroscopic parameters of the ions, but also on the detection system, thus it needs to be experimentally calibrated. Based on this dependence, the intensity ratio between both two levels can be used as an indication of temperature.

If the emissions from both sublevels were not entangled, R_2 emission would appear at lower wavelengths (higher energies) and would gain a larger population with temperature than R_1. However, from the expected position of the transitions shown in Figure 6A (orange and pink lines) and the spectral changes in Figure 8A, it can be concluded that the emissions from R_1 and R_2 to the different sublevels of $^4I_{11/2}$ state are intermixed. Still, it is possible to separate spectral ranges in which one of the sublevels predominates. On doing so, it should be noted that pink and orange lines in Figure 6A are calculated from bulk data and thus cannot be taken as accurate in nanoparticles. Indeed, the increased intensity expected from R_2 at higher temperatures suggests that emission lines are slightly blue-shifted in nanoparticles (roughly 4 nm).

Considering this, spectra measured at different temperatures have been systematically analysed, integrating different spectral ranges to deduce the best calibration for the thermal sensor. In particular, the exact limits of each range and the number of spectral peaks considered to define R_1 and R_2 have been computationally optimized. A summary chart of the different options considered with the integration ranges that provide the best results is offered in Figure 8B. The best option found to minimize uncertainty (best fit to the expected physical law) and to improve relative sensitivity (calculated at 35 °C) appears in Figure 8A as a grey shaded area, and the obtained thermal dependency is plotted in Figure 8C,D. The error bars have been obtained as the standard deviation of seven repetitive measurements performed by moving the sample out of the sample holder and back to its position.

In conclusion, there are two options that appear to be roughly equivalent (in green in Figure 8B), thus we choose the simpler one (framed in green). Accordingly, the best ratio is defined by one integration range for the lower state, R_1 (1036 nm to 1042 nm) and two for the upper state, R_2 (1000–1033 nm and 1047–1082 nm). The spectral regions not included in the ratios are thought to have a stronger extent of mixing, and including them only brings poorer results.

If we consider that in the selected ranges emission entanglement from both sublevels is minimal, we can fit Equation (1)

to the experimental data in Figure 8C. This gives a value of $\Delta E = 170\ cm^{-1}$, which is larger than that reported for the bulk ($113\ cm^{-1}$).[50] Due to the increased concentration of defects in the nanoparticles, and the fact that lattice parameters (Table 1) are also slightly different than those in bulk, this calculated ΔE seems reasonable. However, given the states' entanglement and the fact that the purity of the defined ranges cannot be guaranteed, it cannot be taken as a definitive value.

Nevertheless, the value $170\ cm^{-1}$ can be used as a reference to explore the thermal range in which the material will perform the best, as pointed out in a theoretical work by M. Suta and A. Meijerink.[52] This is so because there is an optimal temperature, T_{opt}, in which a thermometer based on a Boltzmann distribution operates with its largest relative sensitivity. This temperature is given by $T_{opt} = \Delta E/2k_B$, thus it is only dependent on E. Here, this optimal temperature is ≈123K. Considering that CaF_2 does not display any phase change at atmospheric pressure when temperature is reduced and that optical centers are kept,[49,53] it is possible that the nanoparticles could be suited for cryogenic experiments upon thermal calibration. At higher temperatures, the process in which the lower state donates population to the upper one starts saturating, which unavoidably lowers relative and absolute sensitivities. Despite this fact, as shown in Figure 8C, the nanothermometer is functional in the biomedical range.

Considering that entanglement can be stronger than what we can see, we have also considered as a possible calibration curve the simpler linear fit in Figure 8D, which does not assume a specific ΔE. From the application point of view, a sensor defined by a known physical law, like the one in Equation (1), is advantageous, as predictions can be made regarding the effect of stimuli different than temperature on the calibration curve.[2] The linear fit, instead, is not as robust, as it is not known which physical parameters are affecting the slope and the intercept, which may become an inconvenience when performing in complex, harsh environments that require in situ recalibration. Still, it keeps the self-referenced characteristic of ratiometric thermometers, a great advantage of thermometry based on intensity ratios, and thus it also deserves to be considered.[54]

A quality figure of a sensor is sensitivity, *S*, defined as the derivative of the indication with respect to temperature. If normalized by the value of the indication at a certain temperature, the relative sensitivity, S_r, is calculated instead, which can be used to compare with different types of thermometers.[7] Here, the exponential Boltzmann-based fit offers a S_r of 0.27% $°C^{-1}$ at 37 °C ($S = 1.3\%\ °C^{-1}$), while the linear fit provides a S_r of 0.26% $°C^{-1}$ at the same temperature ($S = 1.3\%\ °C^{-1}$). These values are in the range of previously reported sensitivities for this same material, but this new, clearer analysis will help export the thermometer to different situations and sensors.[25] The thermal resolution in these experiments is 0.4 K using the Boltzamm fit, and 1.5 K in the linear fit, being the difference given by the previously measured standard deviation.[55]

Upon $[Y^{3+}]$ increase, the distribution of optical centers changes and is dominated by clusters for $[Y^{3+}] > 10$ mol%. To benefit from the improved intensity caused by the incorporation of Y^{3+}, the intensity ratios need to be optimized in each case, which we have done following the same procedure as in the low Y^{3+} content case. The process has been followed for the two main excitation wavelengths identified, 798 nm, which gives a type-B spectrum, and 792 nm, which gives a type-A spectrum. **Figure 9**A,B shows emission spectra at different temperatures for each excitation. From the spectra, it is apparent that favoring type-B lineshapes with the excitation provides an improved thermal variation. To obtain the best fit in each case, like previously, different options have been considered in terms of integrating ranges and number of components, as in Figure 8B (equivalent figures are shown in Figure S11, Supporting Information). Here, though, we are only using the linear fit, as the contributions of the different optical centers are too overlapped to assume a dependency led by a Boltzmann distribution. The calibration curves obtained are plotted in Figure 9C.

The obtained sensitivity in both cases is lower than that for the sample without Y^{3+}, though it is still in the range of the available thermometers with equivalent characteristics. Specifically, the best S_r obtained is 0.14% $°C^{-1}$ at 798 nm, and 0.10% $°C^{-1}$ at 792 nm, which gives a thermal resolution of 2 and 10 K, respectively. Thus, we can see that type-B lineshape (798 nm excitation) is a better option for thermometry than type-A. Despite this strategy presenting a lower S_r than that based on L-centres, the ten-fold increase in emission intensity in this second approach is key from the application point of view. Such intensity improvement directly translates into a better signal-to-noise ratio, which can relate to the precision with which the intensity ratio can be determined in an experiment.

2.4. Applicability in Biomedicine

In biomedical environments, where excitation power must be limited to avoid tissue damage, higher emission intensity is a clear advantage. Alternatively, higher emission intensity may also help in scenarios requiring reduced acquisition times, as stronger signals allow for shorter integration time in the detector. The International Commission on Non-ionizing Radiation Protection (ICNIRP) recommends that continuous skin exposure at 800 nm should be done at irradiances below $0.3\ W\ cm^{-2}$; however, if exposure is shorter than 10s, irradiance can be increased to $31\ W\ cm^{-2}$.[56] In vitro applications are less restrictive, and depending on the cell line, power densities in the order of $1000\ W\ cm^{-2}$ at this same wavelength can still ensure a high cell viability (irradiation time also plays a role, here).[57] To assess the applicability of the studied nanothermometers, it should be considered that the calibrations shown in Figures 8 and 9 were performed at $1.7\ W\ cm^{-2}$, with 30 s integration time and averaging three spectra. However, the light detection system also plays a role here and needs to be considered (in terms of sensitivity and light collection), which complicates comparison.

Excitation intensity is not the only constraint when nanothermometers are transferred to the biomedical environment. Even in the near-infrared range, tissue autofluorescence and light scattering can generate luminescent backgrounds that hinder accurate temperature measurements.[1] To investigate this effect, we conducted a series of experiments under reduced signal-to-noise ratios and with an overlapping luminescent background (Figure S12, Supporting Information). These experiments demonstrate that the presence of an asymmetric spectral background can compromise measurement precision. Nonetheless, the development

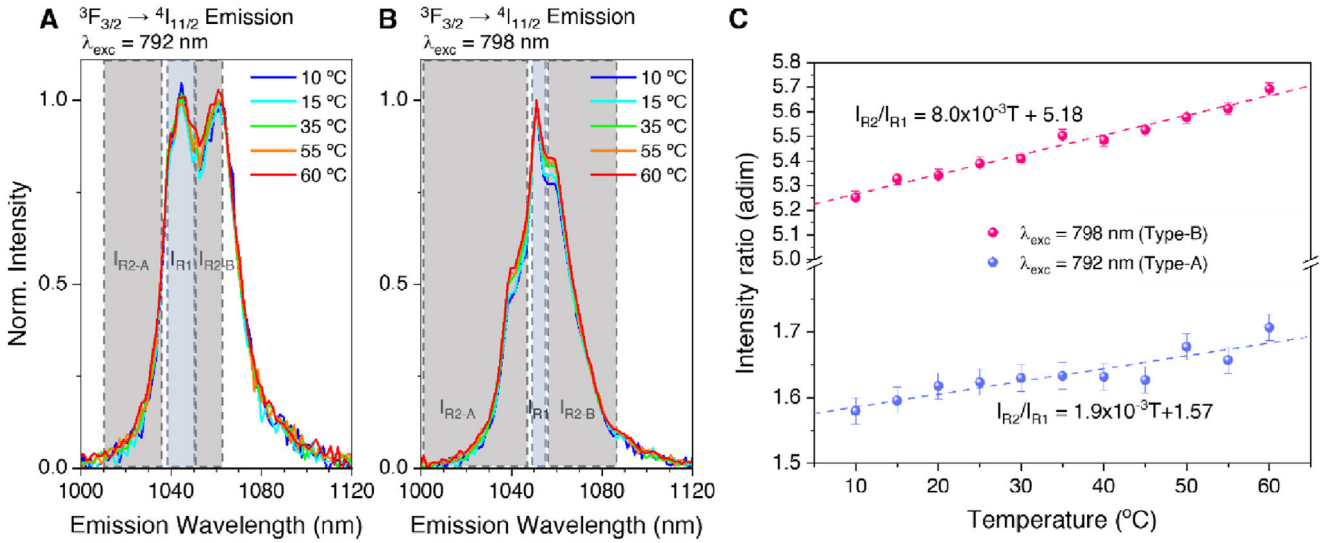

Figure 9. Evaluation of the thermometric options for the $[Y^{3+}] = 15$ mol% sample. Emission spectra recorded at several temperatures are shown under excitation at 792 nm (type-A spectrum) in (A) and at 798 nm (type-B spectrum) in (B). The shaded areas in the graphs indicate the integrating areas found to be the best choice to define the thermometer in each case. The obtained calibration curves are plotted in (C).

of robust data analysis protocols and the use of statistical methods allow for obtaining accurate thermal data.

These findings are significant to biomedical contexts, underlining the relevance of understanding the recorded spectrum to establish adequate analytical protocols. Furthermore, they highlight the need to carefully adjust power density so as not to damage the sample while maintaining suitable signal-to-noise ratios. Unless transient thermal readings are needed, a practical strategy involves performing repetitive measurements and averaging results, as statistical treatment improves accuracy. In such cases, if integration time is kept under safe limits, higher power densities can be used without causing damage (INCIRP sets limits to repetitive irradiations that should also be considered).

Finally, we aim to provide context for the quality of the obtained nanothermometers. As thermal resolution depends on the experimental setup, we use relative sensitivity to compare our results with other works. All materials discussed here are summarized in Table S2 (Supporting Information). In the development of nanothermometry, Er^{3+}/Yb^{3+} based materials have been key. However, their emission lies in the visible region and thus has a limited penetration depth in tissues. Additionally, using Yb^{3+} as sensitizer forces the use of 920 or 980 nm wavelength as excitation, which is strongly absorbed by water and thus, can easily heat the sample. Here, we focus on systems with both their excitation and emission wavelength within the biological windows, as this increases penetration depth and minimizes tissue heating.

Most published alternatives use near-infrared ratios based on the emission bands of two different ions (often Er^{3+} and Ho^{3+}), typically excited through Yb^{3+}.[58–61] The obtained sensitivities are in general within the same range as those obtained here (from 0.005 to 0.25%K^{-1}) with two outstanding exceptions reaching 0.7 and 1.6%K^{-1}.[58,59] Unfortunately, besides the already mentioned limitations that sensitizing with Yb^{3+} involves, Er^{3+}/Ho^{3+} ratios require measuring two spectra, one in the second biological window and another one in the third one, which in certain applications may become a practical problem in terms of detecting system and spectral distortion due to distinct absorption of the tissue.

Alternatively, lanthanides can also be combined with other materials, forming hybrid systems that achieve nanothermometry with a spectral width limited to one biological window.[62,63] As a main advantage, these designs include components that enhance relative sensitivities to values as high as 4.5–7.5%K^{-1}.[63] This, though, happens at the expense of more complex synthetic methods and often larger dimensions of the probes, which can also involve problems in the biomedical field. However, the larger sensitivity makes them particularly interesting if small changes in temperature are expected.

Keeping a narrower spectrum, Yb^{3+}/Nd^{3+} co-doped nanoparticles are a relevant alternative to be considered.[64,65] These are undoubtedly interesting choices that exploit the advantages of the narrow bands of lanthanides. Opposite to the traditional Er^{3+}/Yb^{3+} strategy, here Yb^{3+} is used as an emitter to form a Nd^{3+}/Yb^{3+} interband intensity ratio. The relative sensitivities in this case range between 0.08 and 0.4%K^{-1}. On the downside, part of Yb^{3+} emission still overlaps with the absorption bands of water, meaning that in biological applications, the thermal probe can warm up the surroundings, an effect that must be controlled. From this perspective, narrower bands fully within the low attenuation window simplify the measuring task and prevent unwanted heating. This is the case of the $^3F_{3/2} \rightarrow {}^4I_{11/2}$ transition of neodymium at ≈1042 nm. Indeed, the group of materials strictly working within this range is small, and largely formed by the few Nd^{3+}-doped materials in which this intense emission band can be used for thermometry.[44,45] Relative sensitivities are in the range of those obtained here, as they are restricted by the energetic proximity of the involved emission levels. As an additional example that fulfills the requisites of being within the second biological window and having a narrow emission band, we should also mention PbS/CdS/ZnS quantum dots emitting at 1200 nm

to the list, as the main alternative to lanthanides. The authors do not report relative sensitivity, but they report an absolute sensitivity of 1.0%K^{-1} (In the present work, absolute sensitivity varies from 0.8 to 1.3%K^{-1}).[66,67]

With this summary, it becomes clear that better relative sensitivities exist at the expense of other complexities. Within the range of narrow band emitters, in the applications in which this is required, reported sensitivities are close to the sensitivity of CaF_2:Nd^{3+},Y^{3+} thermometers, which validates the obtained values.

3. Conclusion

The presence of Y^{3+} ions in CaF_2:Nd^{3+},Y^{3+} nanoparticles helps improve the emission intensity from Nd^{3+} at all considered near-infrared wavelengths. However, they also create strong modifications in the spectral lineshape. Such changes are motivated by the creation of more complex optical centers (clusters), labelled as M' and N'. The excitation and emission characteristics of these centers are different enough to allow tuning them even at room temperature. Indeed, modifications on the excitation wavelength as small as 2 nm may have a profound impact on the obtained emission. This is true in terms of emission intensity, but also for the thermometric abilities of the material. The fact that several optical centers overlap in the emission band is probably the reason why CaF_2 is one of the very few host materials that allow intraband thermometry with Nd^{3+} at the most intense emission band ($^3F_{3/2} \rightarrow {}^4I_{9/2}$). Given that both the excitation and emission wavelengths involved fall within the biomedical optical windows and thus are optimal for biomedical applications, we have optimized the thermometric performance of the material considering low and high Y^{3+} concentrations, as well as the excitation wavelength. In general, low Y^{3+} concentration yields higher relative sensitivity (S_r of 0.27%K^{-1} for a Boltzmann fit, or 0.26%K^{-1} for a linear fit), although the corresponding emission intensity is lower. Among the options offered by the sample with high Y^{3+} content (15 mol%), we find that exciting at 798 nm is the best alternative, based on relative sensitivity of 0.14%K^{-1} ($S = 0.8\%K^{-1}$) and enhanced emission intensity. Emission intensity is particularly relevant in biomedical contexts, as it aids in mitigating common challenges, such as autofluorescence signal overlap or the need to reduce excitation power.

4. Experimental Section

Materials: During synthesis, milli-Q water was used as the solvent. All the other chemicals were purchased and used without further purification. This includes calcium chloride dihydrate (>99%, Panreac), neodymium(III) chloride hexahydrate (99.9%, Sigma-Aldrich), yttrium(III) chloride hexahydrate (99.99%, Sigma-Aldrich), and ammonium fluoride (98%, Acros) as precursors for the nanoparticles; and sodium citrate tribasic dihydrate (99.0%, Panreac) as a capping agent.

Synthesis Protocol: CaF_2:Nd^{3+},Y^{3+} nanoparticles were synthesized following a hydrothermal route, with minor changes, on the one published by Pedroni et al.[32] Briefly, the synthesis requires preparing an aqueous solution with all the precursors, and then heating it up in a pressurized reactor autoclave for the reaction to take place. Specifically, precursors are chloride salts of calcium and rare-earth, which are added to 10 mL of water in stoichiometric amounts, calculated to get 3.5 mmol of the final material. For the calculations, it has to be considered that rare-earths enter the lattice substituting Ca^{2+} ions and creating an interstitial fluoride ion. Thus, the compositional formula is $Ca_{1-x-y}F_{2+x+y}$:Nd_x,Y_y. The solution is kept under magnetic stirring for 30 min, before 5.8 g of trisodium citrate dissolved in 10 mL of water is gradually added. The mix is left under vigorous stirring overnight, or for a few hours until it gets a milky white appearance. Then, 324 mg of NH_4F dissolved in 7 mL of water are added, triggering a reaction that leaves the solution transparent in a few minutes. After 30 more minutes of stirring, the solution is transferred to the 50 mL PTFE insert of the pressurized reactor autoclave. Once the reactor has been tightly closed, it is placed in a preheated oven at 70 °C. The oven is programmed to raise the temperature at a rate of 20 °/min up to 180 °C, keeping this temperature for 5 H. After cooling down, the resulting brownish-green opaque solution is centrifuged at 800 g for 15 min. The precipitate, mainly containing the nanoparticles, is then redispersed in water and washed twice at 1500 g in the centrifuge for 15–20 min. The precipitate is redispersed in water and sonicated between steps. A small amount of acetone is also added before centrifuging again. Finally, the nanoparticles are redispersed in 5 mL of water and sonicated, forming our storage solution. For long-term storage, the solutions are kept in the dark or dried.

Composition and Morphology: The morphological characterization was performed via TEM (JEOL JEM-1400 Flash) at CBM Severo Ochoa. Crystal structure has been analyzed through XRD (X'pert Pro Theta/2Theta) with the K_α, $\lambda = 0.1546$ nm, wavelength of copper. The final composition of the nanoparticles has been studied through TXRF (Bruker, S2 PicoFox).

Luminescence: Luminescence has been excited with a tuneable Ti: Sapphire laser fed with a 532 nm laser (Millenia eV, Spectra Physics). Light intensity was set at 3.4 W cm^{-3} in preliminary spectroscopy studies, and reduced to 1.7 W m^{-3} in thermal experiments, to avoid laser heating. Excitation was filtered to remove any red luminescence from the sapphire bar. Accurate spectroscopic characterization was recorded on thin films of dried samples sandwiched between glass coverslips, always placed in the same location to guarantee fair intensity comparisons. Emission was recorded at 90° from the excitation, selecting the emission wavelength with a monochromator (ARC SpectraPro 500-i) and recording it with an InGaAs photodiode. Thermal dependencies, instead, were recorded directly with the stored aqueous suspensions of nanoparticles, held in 10 mm optical path cuvettes (quartz, Hellma). Temperature was controlled with a temperature-controlled cuvette holder (Quantum Northwest) and recorded at 90° with a spectrometer (Ocean Insight, NIR Quest). The reasoning behind using these two different schemes is to have a good spectral resolution in spectroscopy studies, while performing thermal experiments in a simpler set-up that better resembles the practical application of optical sensors.

Supporting Information

Supporting Information is available from the Wiley Online Library or from the author.

Acknowledgements

This manuscript has been developed within CNS2023-145169 SAHNDOCAN and CNS2022-135495, funded by MCIN/AEI/10.13039/501100011033 and by the European Union NextGenerationEU/PRTR. The authors would also like to acknowledge the Spanish Ministry of Science, Innovation, and Universities for projects PID2023-151078OB-I00 and PID2024-161381OB-I00.

Conflict of Interest

The authors declare no conflict of interest.

Data Availability Statement

The data that support the findings of this study are openly available in Zenodo at [https://zenodo.org/records/15192106?preview], reference number 15192106.

Keywords

biological windows, luminescence, nanoparticles, optical sensing, thermometry

Received: April 17, 2025
Revised: September 8, 2025
Published online:

[1] J. Lifante, Y. Shen, E. Ximendes, E. Martín Rodríguez, D. H. Ortgies, *J. Appl. Phys.* **2020**, *128*, 171101.
[2] M. Quintanilla, M. Henriksen-Lacey, C. Renero-Lecuna, L. M. Liz-Marzán, *Chem. Soc. Rev.* **2022**, *51*, 4223.
[3] N. J. L. K. Davis, J. R. Allardice, J. Xiao, A. Karani, T. C. Jellicoe, A. Rao, N. C. Greenham, *Mater. Horiz.* **2019**, *6*, 137.
[4] H. Guo, Y. Lu, Z. Lei, H. Bao, M. Zhang, Z. Wang, C. Guan, B. Tang, Z. Liu, L. Wang, *Nat. Commun.* **2024**, *15*, 4843.
[5] V. B. Kumar, S. K. Mirsky, N. T. Shaked, E. Gazit, *ACS Nano* **2024**, *18*, 2421.
[6] C. Würth, S. Fischer, B. Grauel, A. P. Alivisatos, U. Resch-Genger, *J. Am. Chem. Soc.* **2018**, *140*, 4922.
[7] M. Quintanilla, L. M. Liz-Marzán, *Nano Today* **2018**, *19*, 126.
[8] S. Fischer, N. D. Bronstein, J. K. Swabeck, E. M. Chan, A. P. Alivisatos, *Nano Lett.* **2016**, *16*, 7241.
[9] F. Li, L. Tu, Y. Zhang, D. Huang, X. Liu, X. Zhang, J. Du, R. Fan, C. Yang, K. W. Krämer, J. Marques-Hueso, G. Chen, *Nat. Photonics* **2024**, *18*, 440.
[10] M. D. Wisser, S. Fischer, P. C. Maurer, N. D. Bronstein, S. Chu, A. P. Alivisatos, A. Salleo, J. A. Dionne, *ACS Photonics* **2016**, *3*, 1523.
[11] S. Jaiswal, S. Das, P. P. Borah, P. Anand, R. Métivier, A. Patra, *Adv. Opt. Mater.* **2025**, *13*, 2402221.
[12] J.-C. Boyer, F. C. J. M. van Veggel, *Nanoscale* **2010**, *2*, 1417.
[13] J. Zhao, Z. Lu, Y. Yin, C. McRae, J. A. Piper, J. M. Dawes, D. Jin, E. M. Goldys, *Nanoscale* **2013**, *5*, 944.
[14] M. Kaiser, C. Würth, M. Kraft, I. Hyppänen, T. Soukka, U. Resch-Genger, *Nanoscale* **2017**, *9*, 10051.
[15] M. Quintanilla, E. Hemmer, J. Marques-Hueso, S. Rohani, G. Lucchini, M. Wang, R. R. Zamani, V. Roddatis, A. Speghini, B. S. Richards, F. Vetrone, *Nanoscale* **2022**, *14*, 1492.
[16] G. Liu, *Chem. Soc. Rev.* **2015**, *44*, 1635.
[17] X. Y. Chen, H. Z. Zhuang, G. K. Liu, S. Li, R. S. Niedbala, *J. Appl. Phys.* **2003**, *94*, 5559.
[18] M. Quintanilla, I. X. Cantarelli, M. Pedroni, A. Speghini, F. Vetrone, *J. Mater. Chem. C* **2015**, *3*, 3108.
[19] F. T. Rabouw, P. T. Prins, P. Villanueva-Delgado, M. Castelijns, R. G. Geitenbeek, A. Meijerink, *ACS Nano* **2018**, *12*, 4812.
[20] L. Labrador-Páez, U. Kostiv, J. Widengren, H. Liu, *Adv. Opt. Mater.* **2023**, *11*, 2200513.
[21] M. Quintanilla, N. O. Núñez, E. Cantelar, M. Ocaña, F. Cussó, *J. Appl. Phys.* **2013**, *113*, 174308.
[22] I. Iparraguirre, J. Azkargorta, J. Fernández, R. Balda, A. Oleaga, A. A. Kaminskii, *J. Opt. Soc. Am. B* **1999**, *16*, 1439.
[23] D. Jiang, Y. Zhan, Q. Zhang, F. Ma, L. Su, F. Tang, X. Qian, J. Xu, *CrystEngComm* **2015**, *17*, 7398.
[24] J. Zhu, L. Zhang, J. Zhang, Z. Gao, J. Wang, Z. Wei, L. Su, J. Xu, *2015 11th Conference on Lasers and Electro-Optics Pacific Rim*, IEEE, Busan (South Korea) (CLEO-PR), **2015**, pp. 1.
[25] M. Quintanilla, Y. Zhang, L. M. Liz-Marzán, *Chem. Mater.* **2018**, *30*, 2819.
[26] J. Liu, F. Artizzu, M. Zeng, L. Pilia, P. Geiregat, R. V. Deun, *Photonics Res.* **2021**, *9*, 2037.
[27] M. Zhao, A. Sik, H. Zhang, F. Zhang, *Adv. Opt. Mater.* **2023**, *11*, 2202039.
[28] M. Quintanilla, I. García, I. de Lázaro, R. García-Alvarez, M. Henriksen-Lacey, S. Vranic, K. Kostarelos, L. M. Liz-Marzán, *Theranostics* **2019**, *9*, 7298.
[29] A. Benayas, E. Hemmer, G. Hong, (Eds. D. Jaque García) *Near Infrared-Emitting Nanoparticles for Biomedical Applications*, Springer Suiza **2020**.
[30] Z. Sun, B. Mei, W. Li, X. Liu, L. Su, *Opt. Mater.* **2017**, *71*, 35.
[31] J. A. Sanz-García, G. Lifante-Pedrola, J. E. M. Santiuste, E. Cantelar, *J. Alloys Compd.* **2025**, *1010*, 177529.
[32] M. Pedroni, F. Piccinelli, T. Passuello, S. Polizzi, J. Ueda, P. Haro-González, L. Martinez Maestro, D. Jaque, J. García-Solé, M. Bettinelli, A. S. Water, *Cryst. Growth Des.* **2013**, *13*, 4906.
[33] L. B. Kiss, J. Söderlund, G. A. Niklasson, C. G. Granqvist, *Nanostruct. Mater.* **1999**, *12*, 327.
[34] E. Cantelar, G. Lifante-Pedrola, M. Quintanilla, J. A. Sanz-García, F. Cussó, *J. Alloys Compd.* **2023**, *954*, 170192.
[35] M. Bravo, S. Yang, D. Wen, S. Krzyzowska, F. Taemaitree, S. Zaman, B. Fortuni, S. Rocha, P. Mulvaney, H. Uji-i, S. Brooke, J. Hutchison, *Biorxiv Prepr.* **2024**, https://doi.org/10.1101/2024.02.08.579538.
[36] M. Pedroni, P. Cortelletti, I. X. Cantarelli, N. Pinna, P. Canton, M. Quintanilla, F. Vetrone, A. Speghini, *Sens. Actuators, B* **2017**, *250*, 147.
[37] A. Benayas, B. del Rosal, A. Pérez-Delgado, K. Santacruz-Gómez, D. Jaque, G. A. Hirata, F. Vetrone, *Adv. Opt. Mater.* **2015**, *3*, 687.
[38] S. Acosta, L. J. Borrero-González, P. Umek, L. A. O. Nunes, P. Guttmann, C. Bittencourt, *Sensors* **2021**, *21*, 5306.
[39] L. Marciniak, A. Pilch, S. Arabasz, D. Jin, A. Bednarkiewicz, *Nanoscale* **2017**, *9*, 8288.
[40] U. Rocha, C. Jacinto da Silva, W. F. Silva, I. Guedes, A. Benayas, L. Martínez Maestro, M. A. Elias, E. Bovero, F. C. J. M. van Veggel, J. A. García Solé, D. Jaque, *ACS Nano* **2013**, *7*, 1188.
[41] I. E. Kolesnikov, E. V. Golyeva, A. A. Kalinichev, M. A. Kurochkin, E. Lähderanta, M. D. Mikhailov, *Sens. Actuators, B* **2017**, *243*, 338.
[42] N. Rakov, G. S. Maciel, *J. Appl. Phys.* **2017**, *121*, 113103.
[43] J. Zheng, P. Du, R. An, Y. Liang, Y. Wei, S. Liu, X. Wang, P. Lei, S. Song, H. Zhang, *ACS Appl. Mater. Interfaces* **2025**, *17*, 3578.
[44] C. Renero-Lecuna, A. Herrero, D. Jimenez de Aberasturi, M. Martínez-Flórez, R. Valiente, M. Mychinko, S. Bals, L. M. Liz-Marzán, *J. Phys. Chem. C* **2021**, *125*, 19887.
[45] A. Skripka, A. Morinvil, M. Matulionyte, T. Cheng, F. Vetrone, *Nanoscale* **2019**, *11*, 11322.
[46] J. Corish, C. R. A. Catlow, P. W. M. Jacobs, S. H. Ong, *Phys. Rev. B* **1982**, *25*, 6425.
[47] Y. K. Voron'Ko, A. A. Kaminskii, V. V. Osiko, Analysis of the optical spectra oa CaF2 : Nd3+ (Type 1) crystals, Soviet Physics JETP, **1966**, *22*, 295.
[48] M. Suta, Ž. Antić, V. Đorđević, S. Kuzman, M. D. Dramićanin, A. Meijerink, *Nanomaterials* **2020**, *10*, 543.
[49] F. K. Ma, Q. Zhang, D. P. Jiang, L. B. Su, Y. J. Shao, J. Y. Wang, F. Tang, J. Xu, P. Solarz, W. Ryba-Romanowski, R. Lisiecki, B. Macalik, *Laser Phys.* **2014**, *24*, 105703.
[50] T. P. J. Han, G. D. Jones, R. W. G. Syme, *Phys. Rev. B* **1993**, *47*, 14706.
[51] Y. K. Voron'Ko, R. G. Mikaelyan, V. V. Osiko, *Sov. Phys. JETP* **1968**, *26*, 318.
[52] M. Suta, A. Meijerink, *Adv. Theory Simul.* **2020**, *3*, 2000176.
[53] C. Cazorla, D. Errandonea, *J. Phys. Chem. C* **2013**, *117*, 11292.

[54] S. Balabhadra, M. L. Debasu, C. D. S. Brites, R. A. S. Ferreira, L. D. Carlos, *J. Phys. Chem. C* **2017**, *121*, 13962.
[55] M. D. Dramićanin, *A Rev. Methods Appl. Fluoresc.* **2016**, *4*, 042001.
[56] I. C. N.-I. R. Protection, *Health Phys.* **2013**, *105*, 271.
[57] P. Camarero, P. Haro-González, M. Quintanilla, *Opt. Mater.* **2023**, *142*, 114055.
[58] S. Sekiyama, M. Umezawa, S. Kuraoka, T. Ube, M. Kamimura, K. Soga, *Sci. Rep.* **2018**, *8*, 16979.
[59] M. Jia, Z. Fu, G. Liu, Z. Sun, P. Li, A. Zhang, F. Lin, B. Hou, G. Chen, *Adv. Opt. Mater.* **2020**, *8*, 1901173.
[60] X. Wu, Y. Yu, K. Li, M. Huang, Z. Fu, *J. Lumin.* **2024**, *275*, 120783.
[61] M. Yangui, K. Saidi, C. Hernández-Álvarez, M. Dammak, I. R. Martín, *J. Alloys Compd.* **2025**, *1010*, 177958.
[62] E. N. Cerón, D. H. Ortgies, B. del Rosal, F. Ren, A. Benayas, F. Vetrone, D. Ma, F. Sanz-Rodríguez, J. G. Solé, D. Jaque, E. M. Rodríguez, *Adv. Mater.* **2015**, *27*, 4781.
[63] D. Li, M. Jia, T. Jia, G. Chen, *Adv. Mater.* **2024**, *36*, 2309452.
[64] E. C. Ximendes, W. Q. Santos, U. Rocha, U. K. Kagola, F. Sanz-Rodríguez, N. Fernández, A. d. S. Gouveia-Neto, D. Bravo, A. M. Domingo, B. del Rosal, C. D. S. Brites, L. D. Carlos, D. Jaque, C. Jacinto, *Nano Lett.* **2016**, *16*, 1695.
[65] Ł. Marciniak, A. Bednarkiewicz, M. Stefanski, R. Tomala, D. Hreniak, W. Strek, *Phys. Chem. Chem. Phys.* **2015**, *17*, 24315.
[66] T. Chihara, M. Umezawa, K. Miyata, S. Sekiyama, N. Hosokawa, K. Okubo, M. Kamimura, K. Soga, *Sci. Rep.* **2019**, *9*, 12806.
[67] E. C. Ximendes, U. Rocha, B. del Rosal, A. Vaquero, F. Sanz-Rodríguez, L. Monge, F. Ren, F. Vetrone, D. Ma, J. García-Solé, C. Jacinto, D. Jaque, N. Fernández, *Adv. Healthcare Mater.* **2017**, *6*, 1601195.